scientific reports

Check for updates

OPEN

Investigation of a staggered dual-rotor wound field synchronous motor for offshore wind turbine full-scale testing platforms

Yang Xue[1], Shiyao Qin[2], Chen Qi[2], Ning Wang[3], Cong Liu[3] & Wenliang Zhao[3]✉

The development of high-fidelity testing platforms for offshore wind turbines necessitates drag motors capable of emulating complex marine operating conditions while maintaining ultralow torque ripple. This paper proposes a staggered dual-rotor wound field synchronous drag motor (WFSDM) system for 25 MW full-scale land-based testing platforms targeting large-capacity offshore wind turbines. The research follows a structured approach: firstly, the theoretical model of the WFSDM is introduced, and its dimensions and structural parameters are determined according to design requirements using the D^2L method. To enhance average torque and minimize torque ripple, the rotor structure undergoes further optimization through a multi-objective genetic algorithm. Following this, an analysis of the electromagnetic performance of the optimized WFSDM is conducted. To meet the testing requirements of 25 MW wind turbines, a staggered salient poles assembly of dual-rotor is proposed, which reduces torque ripple to 1.31% while maintaining an average torque output of 34.82 MNm. Finally, the mechanical analysis results are verified to ensure that both the stator and rotor structures comply with safety requirements and possess sufficient safety factors. The staggered dual-rotor WFSDM addresses critical challenges in offshore turbine testing and provides a scalable solution for next-generation offshore wind technology validation, bridging the gap between laboratory testing and real-world marine deployment.

Keywords Electromagnetic performance, Full-scale land-based testing platform, High torque, Low speed, Offshore wind turbines, Wound field synchronous drag motors (WFSDM)

The rapid advancement of offshore wind energy technology has become a cornerstone of global decarbonization strategies[1,2]. With the fast growth in turbine capacities now exceeding 15 MW[3,4]the demand for reliable full-scale validation systems capable of replicating extreme marine operational conditions—such as dynamic wave loads, salt spray corrosion, and grid frequency fluctuations—has become critical[5]. Full-scale land-based testing platforms have thus emerged as indispensable tools in this process[6,7]. These platforms simulate the operational conditions of offshore wind turbines, allowing for comprehensive testing and optimization of various components and systems[8,9]. Their significance lies in accelerating the development of large-capacity offshore wind technology, mitigating deployment risks, and facilitating the widespread adoption of offshore wind energy[10,11]. By providing a controlled environment for testing, these platforms enable engineers and researchers to identify and address potential issues early in the development cycle, thereby reducing costs and improving the overall performance of offshore wind turbines[12,13].

The structure of the full-scale land-based testing platform for large-capacity offshore wind turbine is complex, as shown in Fig. 1, consisting of two main parts: the large-capacity offshore wind turbine system under test and the supporting testing system[14,15]. The large-capacity offshore wind turbine encompasses key components such as the gearbox, wind turbine generator, and converter[16]while the testing infrastructure integrates a low-speed high-torque shaft simulation system, a five-degree-of-freedom non-torque loading mechanism, and a power grid emulation system[17]. This system is designed to simulate various complex offshore operating conditions and typical grid faults, enabling the measurement of turbine operational data under diverse scenarios and facilitating the evaluation of the performance of key large-capacity offshore wind turbine components[18]. As the core component, the drag motor is tasked with driving the tested offshore wind turbine by precisely controlling

[1]The School of Mechanical Engineering, Tianjin University, Tianjin 300072, China. [2]China Electric Power Research Institute, Beijing 100192, China. [3]The School of Electrical Engineering, Shandong University, Jinan 250061, China. ✉email: wlzhao@sdu.edu.cn

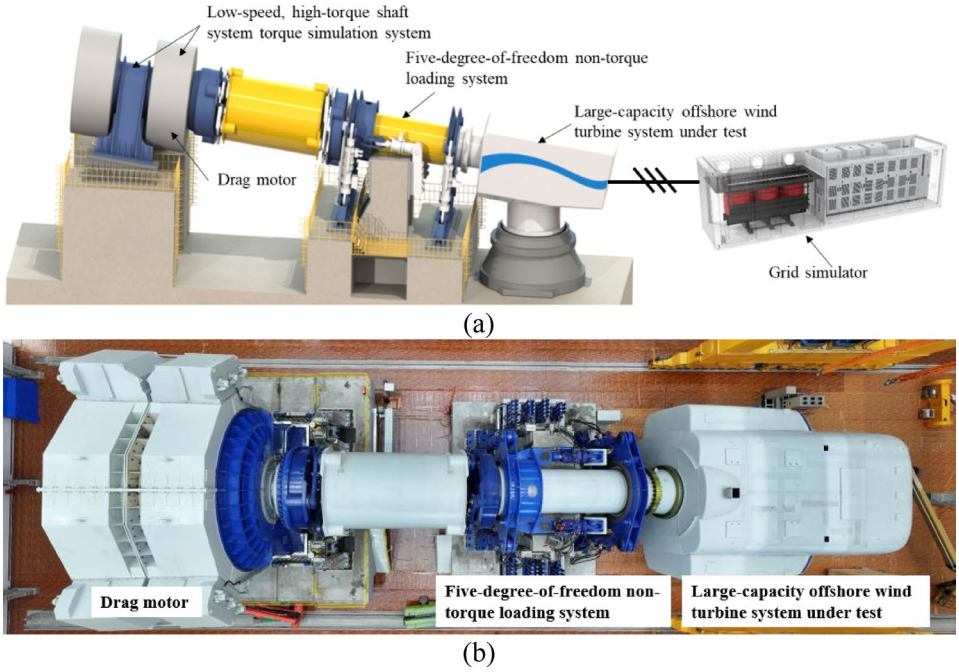

Fig. 1. The full-scale land-based testing platform for large-capacity offshore wind turbine. **a** Model. **b** Investigation test platform, in Fuqing, Fujian Province.

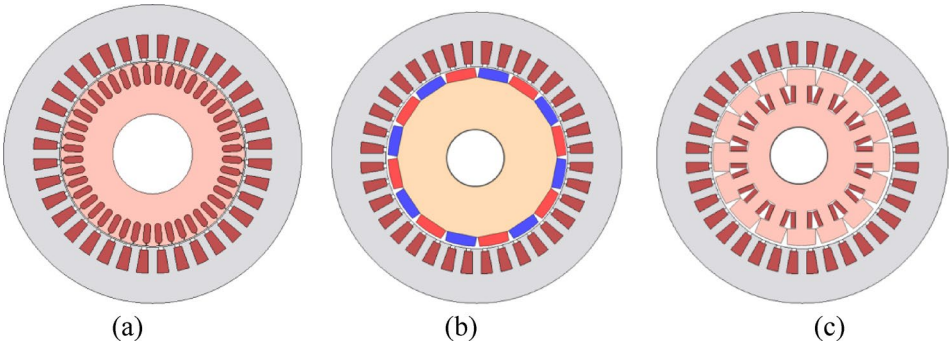

Fig. 2. The main types of high-power drag motors. **a** IDM. **b** PMSDM. **c** WFSDM.

output torque, and it can simulate the dynamic characteristics of the wind turbine generator under different wind speeds and load conditions[19,20].

High-power drag motors mainly include induction drag motors (IDMs)[21]permanent magnet synchronous drag motors (PMSDMs)[22]and wound field synchronous drag motors (WFSDMs)[23]as depicted in Fig. 2. IDMs are widely adopted due to their robustness, dependability, simplicity, and relatively low cost. However, they suffer from efficiency losses stemming from the requirement for reactive power excitation and rotor resistance[24–26]. Additionally, IDMs have lower efficiency at low speeds and high torques, which are typical requirements for simulating the operating conditions of offshore wind turbines. Conversely, PMSDMs offer high efficiency, high power density, and excellent dynamic performance[27]. However, the magnetization and demagnetization of large PMSDMs present significant challenges, and the permanent magnets are also at risk of demagnetization. Furthermore, the cost of permanent magnets is a significant factor, especially for large PMSDMs, which can increase the overall system cost[28]. WFSDMs, alternatively, present a promising alternative that combines the robustness of IDMs with the high-performance capabilities of PMSDMs[29,30]. They utilize an external excitation system to create a magnetic field that synchronizes with the rotor[31]. The ability to dynamically adjust the excitation current enables WFSDMs to maintain optimal performance across a wide range of operating conditions compared to IDMs, making them ideal for simulating the dynamic loads experienced by offshore wind turbines. Moreover, WFSDMs offer better dependability and lower maintenance costs compared to PMSDMs, which further enhances their suitability for full-scale land-based testing platforms. Since the testing platform is built near the wind power plant in Fuqing, Fujian Province, efficiency is not a priority issue. The cost, efficiency and dependability of the three types of drag motors are shown in Table 1.

Items	IDM	PMSDM	WFSDM
Cost	Lowest	Highest	Medium
Efficiency	Medium (85–92%)	Highest (> 97%)	High (> 95%)
Dependability	Highest	Medium	Medium-high

Table 1. Comparison of cost, efficiency, and dependability for three drag motors.

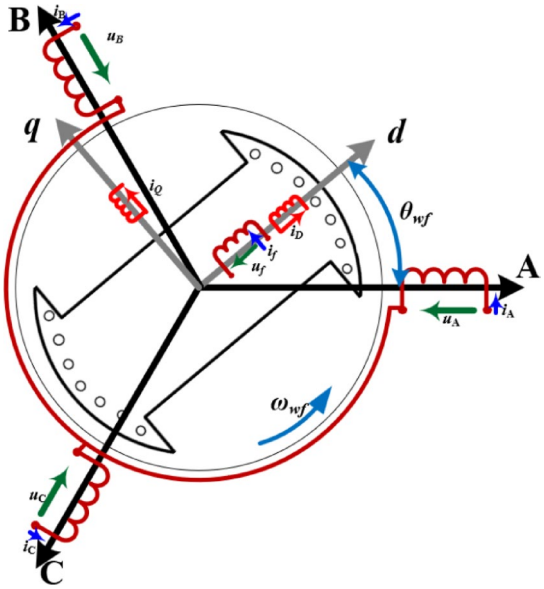

Fig. 3. Physical model of a three-phase WFSDM.

While WFSDMs offer a robust alternative to IDMs and PMSDMs for high-power drag applications, their susceptibility to torque ripple remains a critical barrier in offshore wind turbine full-scale testing platforms. Existing torque ripple suppression strategies for synchronous motors mainly focus on electromagnetic design optimizations and control, such as fractional-slot winding configurations, and harmonic current injection control[32]. However, these methods face inherent limitations in megawatt-scale WFSDMs. Fractional-slot designs increase manufacturing complexity for large pole-count rotors. And the harmonic injection requires precise real-time control, increasing the risk of system instability during the testing of offshore wind turbines. Furthermore, conventional dual-rotor assemblies exacerbate torque ripple due to synchronous pole alignment, directly conflicting with the low torque ripple.

To address this problem, this paper designs a 25 MW staggered dual-rotor wound field synchronous motor for offshore wind turbine full-scale testing platforms. This paper is organized as follows: Sect. "Design of WFSDMs" introduces the theoretical model, design requirements and design flow of WFSDMs. Then in Sect. "Analysis of electromagnetic performance", the rotor parameters of the WFSDM are optimized, the electromagnetic performance of the WFSDM is analyzed, and the staggered salient poles assembly of dual-rotor is proposed to reduce the torque ripple of the drag motor system. This is followed by verifying the structural performance of the drag motor system in Sect. "Drag motor system structure performance" to ensure structural safety. Finally, a conclusion is provided in Sect. "Conclusion".

Design of WFSDMs

Theoretical model of WFSDMs

The physical model of a three-phase WFSDM equipped with damping windings is depicted in Fig. 3. The stator features three symmetrical windings labeled A, B, and C, while the salient-pole rotor incorporates an excitation winding and damping windings. The damping windings consist of direct-axis windings, denoted as D, and quadrature-axis windings, denoted as Q. The damping winding incorporates short-circuited terminals across all segments. For the sake of analysis simplicity, the following assumptions are made: (1). The effect of the stator and rotor surface slots is neglected; (4). The stator three-phase windings are symmetrical; (2). The rotor structure is symmetrical for both the direct-axis and the quadrature-axis; (3). The magnetic circuit is linear; (5). The air-gap magnetic field is distributed sinusoidally in space.

According to Kirchhoff's second law and Faraday's law of electromagnetic induction, the voltage equations for the stator windings are as follows:

$$\begin{cases} u_A = i_A R_{swf} + \frac{d\psi_A}{dt} \\ u_B = i_B R_{swf} + \frac{d\psi_B}{dt} \\ u_C = i_C R_{swf} + \frac{d\psi_C}{dt} \end{cases} \tag{1}$$

where u_A, u_B, and u_C are the voltages of the stator windings in phases A, B, and C, respectively; i_A, i_B, and i_C are the currents of the stator windings in phases A, B, and C, respectively; ψ_A, ψ_B, and ψ_C are the flux linkages of the stator windings in phases A, B, and C, respectively; and R_{swf} is the resistance of each phase of the stator winding. The voltage equations for the excitation winding and the damping windings are as follows:

$$\begin{cases} u_f = i_{fwf} R_{fwf} + \frac{d\psi_f}{dt} \\ u_D = 0 = i_{Dwf} R_{Dwf} + \frac{d\psi_D}{dt} \\ u_Q = 0 = i_{Qwf} R_{Qwf} + \frac{d\psi_Q}{dt} \end{cases} \tag{2}$$

where u_f is the voltage of the excitation winding; u_D and u_Q are the voltages of the *d*-axis and *q*-axis damping windings, respectively, which are zero due to the self-short-circuit of the windings; i_{fwf}, i_{Dwf}, and i_{Qwf} are the currents of the excitation winding and the *d*-axis and *q*-axis damping windings, respectively; and R_{fwf}, R_{Dwf}, and R_{Qwf} are the resistances of the excitation winding and the *d*-axis and *q*-axis damping windings, respectively.

Equations (1) and (2) can be written in matrix form:

$$\begin{cases} \mathscr{u}_s = \mathcal{R}_{swf} \boldsymbol{i}_s + \frac{d}{dt} \boldsymbol{\psi}_s \\ \mathscr{u}_r = \mathcal{R}_{rwf} \dot{\mathscr{r}} + \frac{d}{dt} \psi_r \end{cases} \tag{3}$$

where $\boldsymbol{u}_s$ and $\boldsymbol{u}_r$ are the voltage column vectors of the stator and rotor windings, respectively; $\boldsymbol{i}_s$ and $\boldsymbol{i}_r$ are the current column vectors of the stator and rotor windings, respectively; $\boldsymbol{\psi}_s$ and $\boldsymbol{\psi}_r$ are the flux linkage column vectors of the stator and rotor windings, respectively; $\boldsymbol{R}_{swf}$ and $\boldsymbol{R}_{rwf}$ are the resistance matrices of the stator and rotor windings, respectively.

$$\boldsymbol{u}_s = \begin{bmatrix} u_A & u_B & u_C \end{bmatrix}^T, \boldsymbol{u}_r = \begin{bmatrix} u_f & u_D & u_Q \end{bmatrix}^T,$$

$$\boldsymbol{i}_s = \begin{bmatrix} i_A & i_B & i_C \end{bmatrix}^T, \boldsymbol{i}_r = \begin{bmatrix} i_{fwf} & i_{Dwf} & i_{Qwf} \end{bmatrix}^T,$$

$$\boldsymbol{\psi}_s = \begin{bmatrix} \psi_A & \psi_B & \psi_C \end{bmatrix}^T, \boldsymbol{\psi}_r = \begin{bmatrix} \psi_f & \psi_D & \psi_Q \end{bmatrix}^T,$$

$$\boldsymbol{R}_{swf} = \begin{bmatrix} R_{swf} & 0 & 0 \\ 0 & R_{swf} & 0 \\ 0 & 0 & R_{swf} \end{bmatrix}, \boldsymbol{R}_{rwf} = \begin{bmatrix} R_{fwf} & 0 & 0 \\ 0 & R_{Dwf} & 0 \\ 0 & 0 & R_{Qwf} \end{bmatrix}.$$

The motion equation of WFSDM is:

$$T_e = T_L + \frac{J}{p_n} \frac{d\omega_{wf}}{dt} \tag{4}$$

where J is the moment of inertia of WFSDM; T_L is the total load torque, including frictional resistance torque and elastic torque; T_e is the electromagnetic torque; P_n is pole pair; ω_{wf} represents the rotor angular velocity expressed in electrical angular speed.

The assumptions of a sinusoidal air-gap flux distribution and linear magnetic circuits facilitate the derivation of fundamental voltage and torque equations (Eqs. 1–4). However, under high-load conditions, localized saturation in the stator and rotor teeth distorts the air-gap flux waveform, deviating from the sinusoidal assumption. During highly dynamic situations, excitation winding currents introduce transient harmonics that are not captured by steady-state equations, thereby violating the linear permeability model. Despite these limitations, such simplifications are essential for reducing complexity during the initial sizing design of the WFSDM. Crucially, the subsequent finite element methods (FEM) analysis can rigorously account for saturation effects and slot harmonics. This approach effectively mitigates the adverse effects introduced by the assumptions, ensuring that the final design is robust and reliable under real-world operating conditions.

Design requirements for WFSDMs

To fulfill the testing requirements of a 25 MW offshore wind turbine full-scale testing platforms, its drag system employs two three-phase WFSDMs with identical technical specifications, due to the limitations of space and inverter capacity. They will be connected in coaxial series. Each WFSDM has a rated power of 12.5 MW, a rated voltage of 3.3 kV, a rated speed of 7 rpm, and a speed regulation range of 0–14 rpm. Below the rated speed, constant torque speed regulation is employed, while above the rated speed, constant power speed regulation is used. At rated power, the root mean square (RMS) value of stator current density is no more than 4.5 A/mm^2 and the RMS value of the excitation winding current density is not exceeding 3 A/mm^2. The specific design requirements are listed in Table 2.

In order to improve the torque output performance, the motor adopts a salient pole structure, and the structural parameters of the WFSDMs are referenced to the high-power pumped storage motors. In this design,

Items	Unit	Value
Rated power	MW	12.5
Rated voltage	kV	3.3
Rated speed	rpm	7
Stator current density (RMS)	A/mm^2	≤ 4.5
Excitation winding current density (RMS)	A/mm^2	≤ 3

Table 2. Design requirements for parameters of wfsdms. 2.3 determination of the main structure parameters.

Items	Unit	Value
Rated excitation current	A	2000
Winding type	-	Y
Number of poles/slots		120/540
Air Gap Length	mm	12
Rotor inner diameter	mm	4650
Stator inner diameter	mm	4905
Stator outer diameter	mm	5100
Axis Length	mm	10,400
Excitation winding turns	-	17
Stator winding turns	-	12

Table 3. Main parameters of the wfsdms.

the magnetic loading of the WFSDMs is also referenced to the high-power pumped storage motors initially set at 0.85T, which can be subsequently adjusted according to the magnetic circuit iteration. Due to the use of winding excitation, before starting the calculation, the power factor and efficiency of the motor can be preset to 1 and 0.9, respectively. The main electromagnetic parameters armature diameter, armature core length, motor capacity, rotational speed and the electromagnetic load of the motor are related as follows:

$$\frac{D_{ld}^2 l_{ef} n_{Nwf}}{P_{Nwf}} = \frac{6.1}{a_p K_{NM} K_W A B} \tag{5}$$

where D_{ld} is the armature diameter, l_{ef} is the effective length of the WFSDM, n_{Nwf} is the WFSDM speed, P_{Nwf} is the size of the electromagnetic power of the WFSDM, a_p is the calculation of the pole arc coefficient, K_{NM} is the waveform coefficient of the magnetic field of the air gap, Kw is the winding coefficient, A is the line load of 4.5 A/mm^2, and B is the magnetic load. After the armature is energized under the action of sinusoidal magnetic field, an induced electromotive force will be generated in the three-phase symmetrical windings, which can determine the number of motor excitation winding turns and stator winding turns. The parameters of the WFSDMs shown in Table 3 can be determined by using the design flowchart of WFSDMs shown in Fig. 4. Initially, the main dimensions of the WFSDM are determined using the D^{2}L method. Subsequently, the design process progresses to the stator and stator winding design, followed by the rotor and field winding design. Finally, FEM is employed to validate whether the design meets the design requirements. If the FEM results do not satisfy the design criteria, the process reverts to the D^{2}L method for redetermination of the WFSDM's main dimensions. This iterative procedure continues until the FEM confirms that the design objectives are fully met. In order to reduce the air gap magnetic field harmonics, the stator skew slot is 0.5 tooth pitch.

Analysis of electromagnetic performance

Performance optimization

When designing the 12.5 MW WFSDM, in order to further improve the performance, the nondominated sorting genetic algorithm II (NSGA-II) for multi-objective optimization is carried out by the finite element software. The fitness functions for maximizing the average torque T_{avg} and minimizing the torque ripple T_{rip} are given by

$$\begin{cases} f_1 = \max(T_{avg}) \\ f_2 = \min(T_{rip} = \frac{T\max - T\min}{T_{avg}} \times 100\%) \end{cases} \tag{6}$$

Five design variables, the rotor yoke thickness T_y, rotor tooth height H_t, rotor tooth width W_t, rotor tooth top height H_{tt}, and rotor tooth top radius R_t, are selected as displayed in Fig. 5. As shown in (7), the constraints are designed to avoid severe degradation of T_{rip} and T_{avg}. The limits of the design variables are presented in (8).

$$\begin{cases} T_{rip} \leqslant 7.5\% \\ T_{avg} \geqslant 15\mathrm{MNm} \end{cases} \tag{7}$$

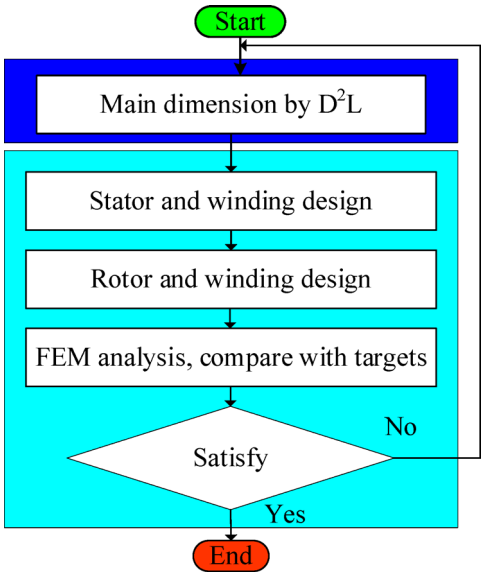

Fig. 4. Design flowchart of WFSDMs.

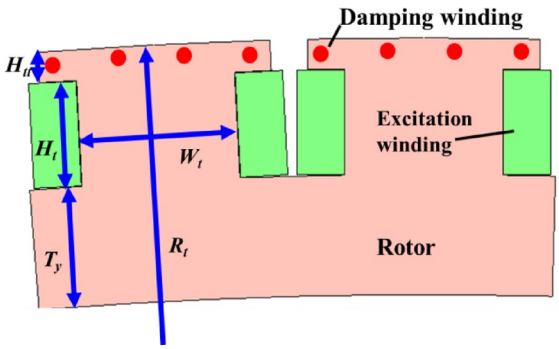

Fig. 5. Optimization variables of rotor.

$$\begin{cases} 110\text{mm} \leqslant T_y \leqslant 120\text{mm} \\ 95\text{mm} \leqslant H_t \leqslant 110\text{mm} \\ 140\text{mm} \leqslant W_t \leqslant 170\text{mm} \\ 25\text{mm} \leqslant H_{tt} \leqslant 30\text{mm} \\ 500\text{mm} \leqslant R_t \leqslant 4000\text{mm} \end{cases} \tag{8}$$

In addition, convergence criteria require the Pareto front improvement to remain below 0.1% over 50 generations while capping maximum generations at 200. And these criteria employed a 100-individual population with 0.9 crossover probability and 0.05 mutation rate. After optimization, the optimal values of T_y, H_t, W_t, H_{tt}, R_t are 113.6 mm, 99 mm, 150 mm, 28.76 mm, and 600 mm respectively. The corresponding values of torque average and torque ripple values are 17.41 MNm and 4.13%, respectively.

Electromagnetic performance

The optimized WFSDM model and corresponding mesh profile are presented in Fig. 6, featuring localized grid refinement in the motor's air gap region to achieve enhanced simulation fidelity. Figure 7 illustrates the stator winding coupling circuit, where e_s and i_s denote the back electromotive force (EMF) and current per phase; R_{1e} and L_{1e} represent the end-winding resistance and leakage inductance of the stator terminals; R_L and L_L correspond to the conductor resistance and inductance within stator slots, respectively. The damping winding coupling circuit, as shown in Fig. 8, incorporates short-circuited terminals across all segments, where i_k, R_{1e} and L_{1e} designate the current, end resistance, and leakage inductance of the kth damping winding segment, respectively; i_{bk}, R_b and u_k correspond to the body current, body resistance, and induced EMF for the kth damper bar segment, respectively.

Given a rated excitation current of 2000 A and a rotational speed of 7 rpm, with no stator current applied, the air gap flux density distribution is depicted in Fig. 9. It is evident that the no-load air gap flux density is distorted in the stator teeth due to the influence of the stator teeth. The harmonic spectrum, obtained from the

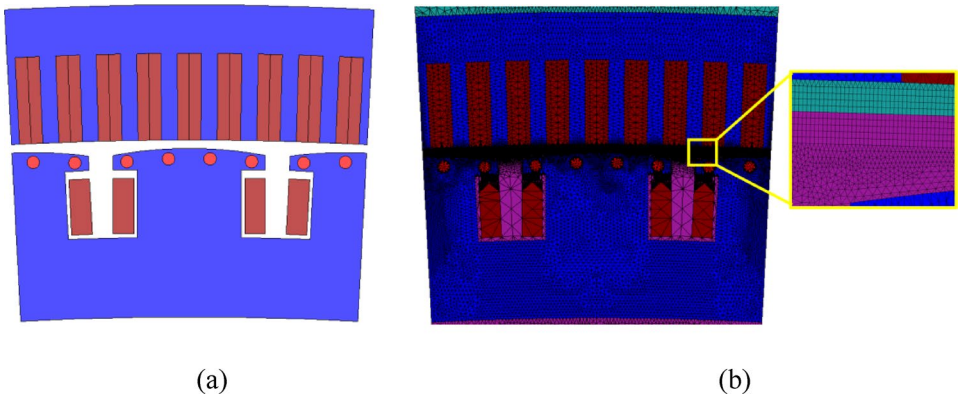

Fig. 6. Optimized WFSDM. **a** Optimized model. **b** Mesh profile.

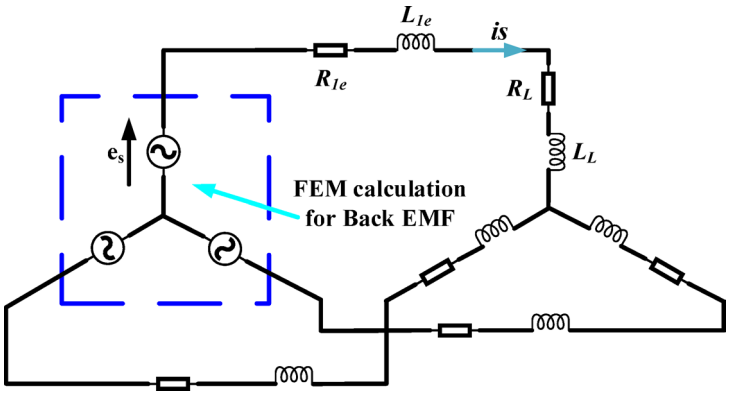

Fig. 7. The stator winding coupling circuit.

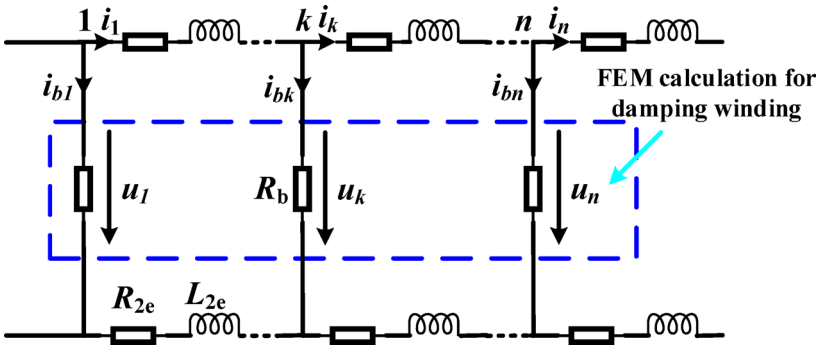

Fig. 8. The damping winding coupling circuit.

FFT analysis of the air gap flux density, reveals that the fundamental amplitude of the air gap flux density is 1.023 T, with the 9th harmonic amplitude being the highest at 0.099 T. The motor's pole and slot configuration, with 60 pole pairs and 540 slots, results in relatively high 7th, 9th, and 11th harmonics of the air-gap magnetic flux density. This is attributed to the specific combination of the number of slots per pole per phase, which can be mitigated by optimizing the pole-slot combination.

The waveform and spectrum of the back EMF are illustrated in Fig. 10. The sinusoidality of the back EMF with a stator skew slot is significantly higher than that of the model without a skew slot. The model without a skew slot exhibits a very high 17th harmonic, while the highest order harmonic in the model with a stator skew slot is the 5th harmonic at 245 V. The total harmonic distortion (THD) of the no-load back EMF is calculated as:

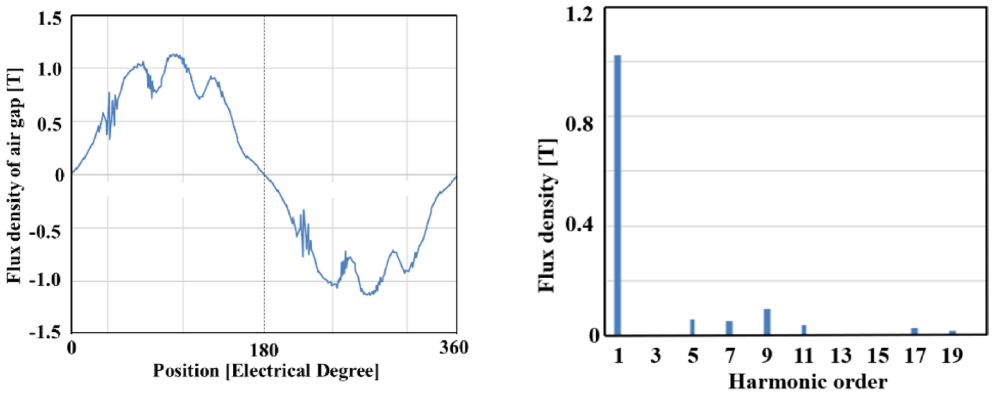

Fig. 9. No-load air gap flux density. **a** Waveform. **b** Spectrum.

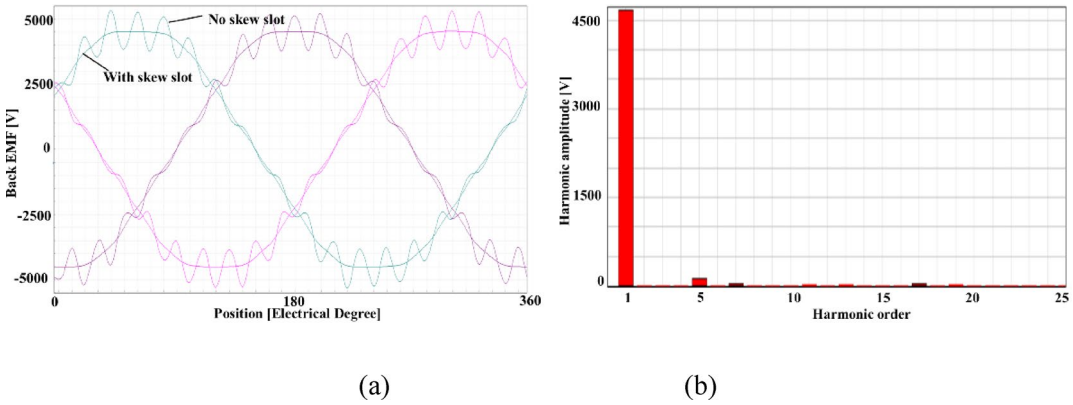

Fig. 10. No-load back electromotive force. **a** Waveform. **b** Spectrum with skew slot.

$$THD = \frac{\sqrt{U_2^2 + U_3^2 + U_4^2 + \cdots\cdots + U_{100}^2}}{U_1} \times 100\% = \ 0.852\% \tag{9}$$

where U_1 is the fundamental RMS value, and U_n ($n>1$) is the nth harmonic RMS value. A high THD in the back EMF can lead to increased torque ripple, causing mechanical vibrations and noise, thereby reducing the overall efficiency and lifespan of the WFSDM. Moreover, WFSDMs with high THD in the back EMF can inject harmonics into the power grid, affecting the overall power quality. However, the THD of the back electromotive force of this motor is less than 1%, which meets the requirements.

With a rated excitation current of 2000 A, a rotational speed of 7 rpm, and a three-phase stator current of 2340 A, the load electromagnetic torque is shown in Fig. 11. The average value of the electromagnetic torque is 17.41 MNm, with a torque ripple of 4.13%. The prototype of the WFSDM is depicted in Fig. 12a.

Torque ripple suppression via staggered salient poles

To achieve a drag capacity of 25 MW, the drag system employs two 12.5 MW WFSDMs with series-connected rotors operating coaxially, as illustrated in Fig. 12b. This configuration doubles the torque output but also increases the torque ripple range of the drag motor system. To ensure stable system operation, it is essential to mitigate the torque ripple. The conventional arrangement of dual rotors is depicted in Fig. 13a. A staggered rotor tooth structure is adopted for the series-connected rotors operating coaxially. Specifically, Rotor A and Rotor B are placed at a 90-electrical-degree (ED) offset, as shown in Fig. 13b. This arrangement interleaves the salient poles of the motor rotors, aligning the salient poles of Rotor A with the slots of Rotor B. Consequently, the peaks and troughs of the torque from the two rotors superimpose, effectively suppressing torque ripple through peak shaving and valley filling.

Under no-load conditions and rated excitation current, the peak-to-peak no-load torque for a single WFSDM rotor is 1.76 MN·m. In a conventional salient-pole dual-rotor assembly, this value doubles to 3.52 MN·m, as evident in Fig. 14a. However, employing a staggered salient-pole dual-rotor assembly allows the torque peaks and valleys from the two rotors to superimpose, thereby reducing the peak-to-peak no-load torque. Specifically,

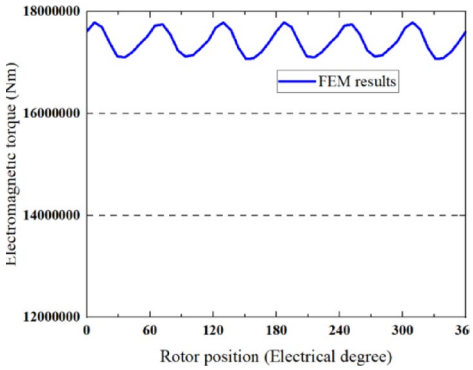

Fig. 11. FEM results of electromagnetic torque.

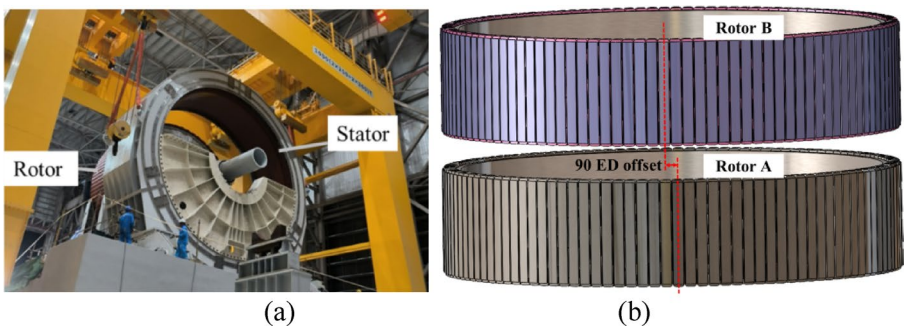

Fig. 12. WFSDM. **a** Prototype. **b** Rotor structure.

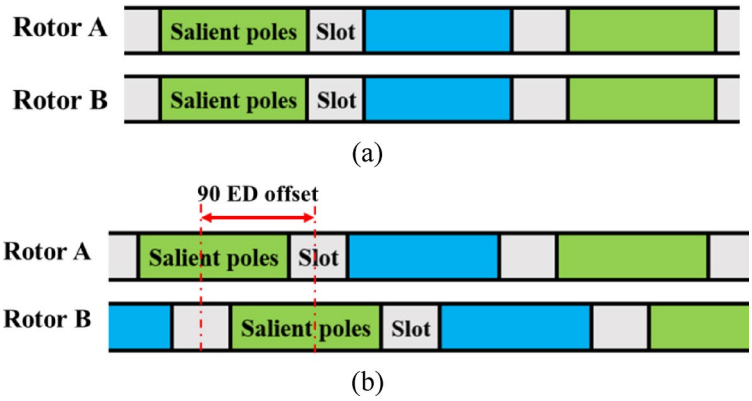

Fig. 13. Dual-rotor structure. **a** Conventional salient poles assembly. **b** Staggered salient poles assembly.

as shown in Fig. 14b, the peak-to-peak no-load torque reduces to 0.48 MN·m, representing an 86.36% decrease compared to the conventional dual-rotor assembly and a 72.73% decrease compared to the single rotor, demonstrating significant suppression.

Under rated load, the single WFSDM rotor achieves a maximum output torque of 17.41 MN·m, with a torque ripple range of 0.72 MN·m and a torque ripple of 4.13%. The conventional salient-pole dual-rotor assembly yields an average torque of 34.82 MN·m and a torque ripple range of 1.44 MN·m, as shown in Fig. 15a. Conversely, the staggered salient-pole dual-rotor assembly achieves the same average torque (34.82 MN·m) but substantially lowers the torque ripple range to 0.46 MN·m and the torque ripple to 1.31%. Compared to the conventional assembly, the output torque is maintained while the torque ripple coefficient is reduced by 2.82%. Fig. 15b illustrates the torque waveform. The experimental results are shown in Fig. 15c, the average value is 34.8 MNm, and the torque fluctuation range is 0.14 MN·m. Due to the current sensor's sampling rate (4 Hz), direct comparison of torque ripple coefficients is impractical; however, the average torque aligns closely with FEM results (< 1% error), attributable primarily to magnetic end leakage and mechanical manufacturing

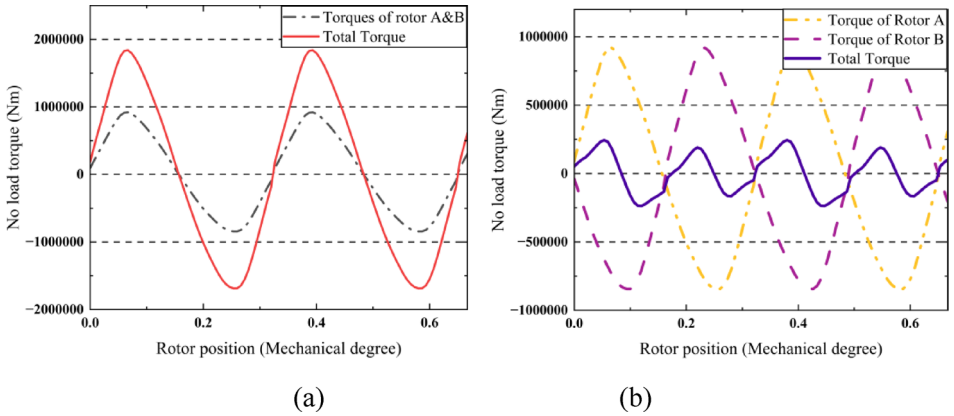

Fig. 14. No-load torque. **a** Conventional salient poles assembly. **b** Staggered salient poles assembly.

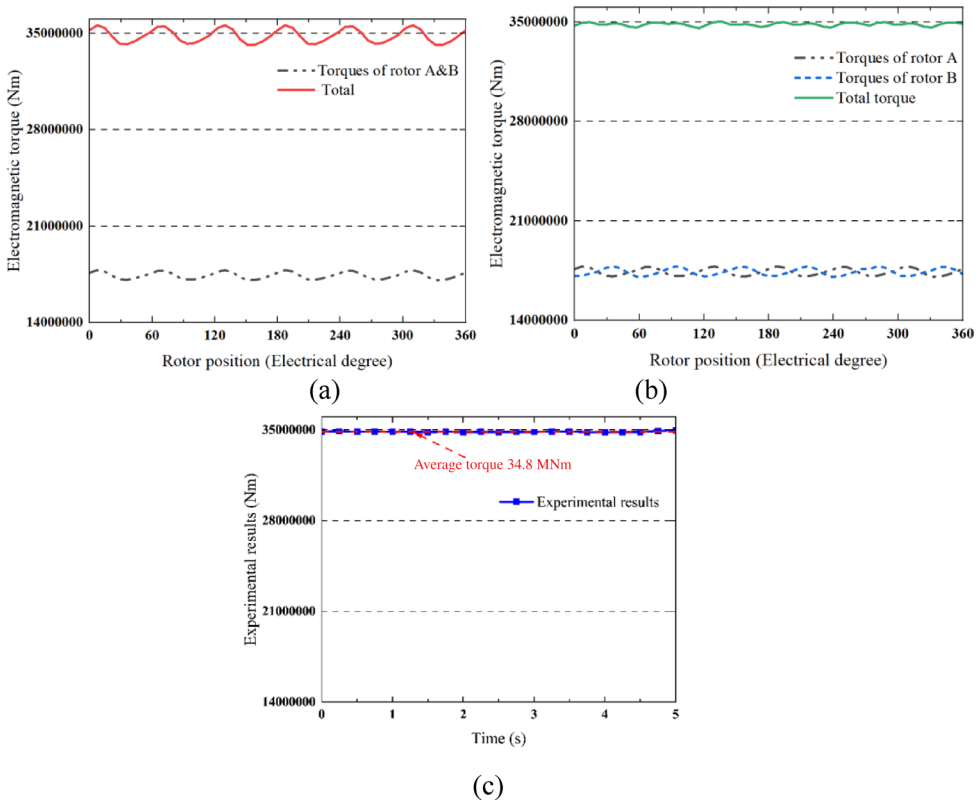

Fig. 15. Electromagnetic torque. **a** FEM results for conventional salient poles assembly. **b** FEM results for staggered salient poles assembly. **c** Experimental results, indirectly calculated through current measurement data.

tolerances. Thus, the staggered salient-pole assembly effectively mitigates both no-load torque and torque ripple in the WFSDM traction motor system while maintaining torque capability, significantly enhancing operational stability. The achieved torque ripple of 1.31% meets experimental equipment requirements. For further reduction, investigating torque ripple suppression control algorithms for the WFSDM is recommended. At rated load and 1.31% torque ripple, the efficiency is 95.83%. This value, calculated as the ratio of mechanical output power to effective electrical input power, aligns with the data in Table 1.

Drag motor system structure performance

Overall structure

The drag motor system employs a horizontal installation method with a dual-shaft extension structure, as shown in Fig. 16. The bearings are segmented hydrostatic sliding bearings, with the driving end utilizing radial thrust

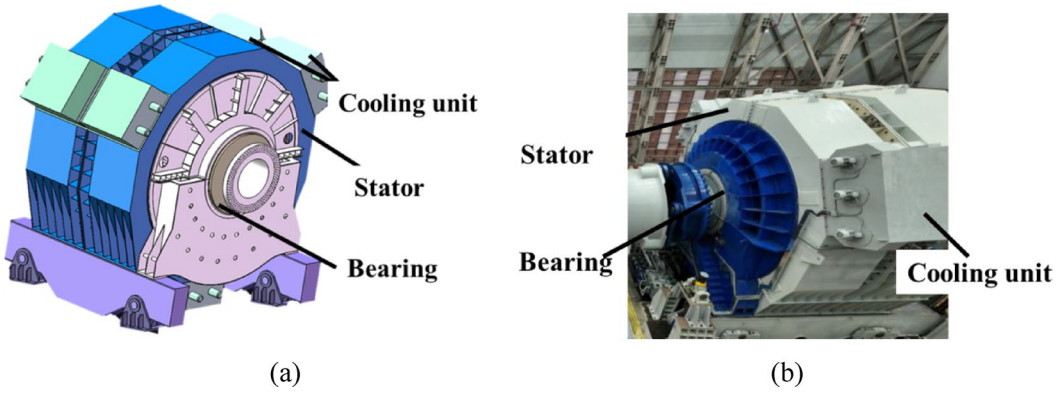

Fig. 16. Overall structure of the drag motor system. **a** 3-D model. **b** Drag motor system.

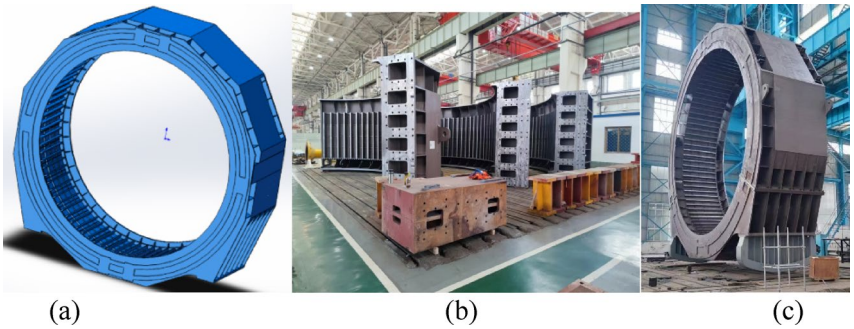

Fig. 17. Stator. **a** 3-D model. **b** Welded parts. **c** Assembled stator.

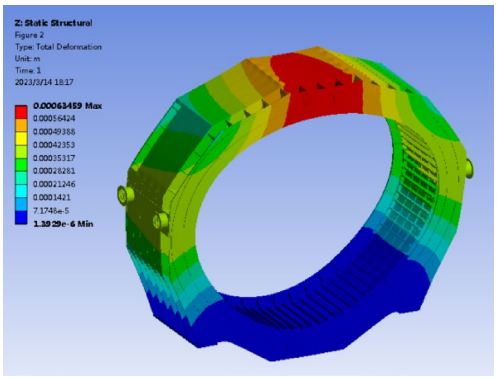

Fig. 18. Deformation of stator under lifting conditions.

bearings capable of enduring 550 tons of radial force and 140 tons of axial thrust. The cooling unit is of a backpack design positioned atop the motor stator, incorporating a leak detection device and drainage holes within. The ventilation system adopts a full radial circulating cooling method. The collector ring and brush holder are arranged at the rear end of the motor, where an encoder mounting interface is also reserved.

Stator structure

The motor stators comprise stator shells, cores, and coils. The shells are fabricated by welding steel plates into three 120° segments, which are then bolted together during assembly, as shown in Fig. 17. To evaluate structural stiffness, deformation and stress analyses of the core and shell were performed. For safe handling during transportation to the test platform, lifting conditions were analyzed, revealing maximum deformations of 0.63 mm that satisfy installation requirements, as seen in Fig. 18. To guarantee the structural integrity of the stator and support structure under the action of rated torque and rotor gravity, an analysis of the deformation and stress of both was performed. As illustrated in Fig. 19, the maximum deformation is 0.62 mm, aligning with

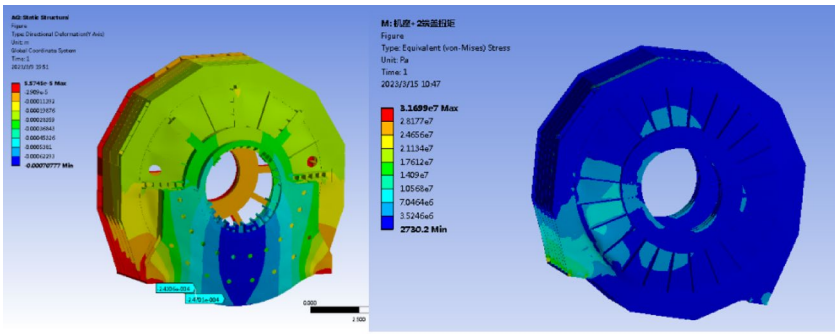

(a) (b)

Fig. 19. Analysis results of stator structure. **a** Deformation. **b** Stress.

Operating condition	Stress	Calculated value (MPa)	Allowable value (MPa)	Safety factor
Rated torque condition	Maximum equivalent stress	32	125	3.9
Short-circuit condition	Maximum equivalent stress	161	375	2.3

Table 4. Results of stator structure analysis for drag motor systems.

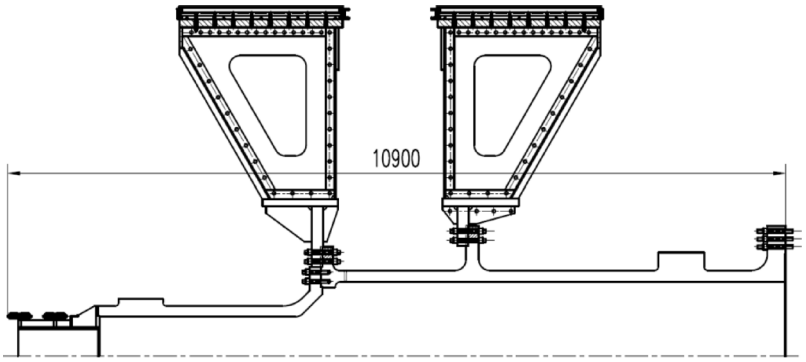

Fig. 20. Rotor structure.

installation specifications. The stator casing is made of carbon structural steel Q235B material, with an allowable stress value of 125 MPa. The Q235B carbon steel stator casing exhibits allowable stress of 125 MPa. Under rated operation, maximum equivalent stress reaches 32 MPa, yielding a 3.9 safety factor that meets requirements, as detailed in Table 4. During short-circuit conditions, maximum equivalent stress is 161 MPa against the material's 375 MPa yield strength, achieving a 2.3 safety factor.

Rotor structure

The rotor of the drag motor system adopts a salient pole structure, with the rotor core secured to the rotor bracket using tension bolts, ensuring a reliable structure, as shown in Fig. 20. The rotor bracket is welded from steel plates, capable of withstanding high torque stresses and frequent start-up fatigue damage, while also facilitating ventilation and heat dissipation. The shaft and rotor bracket are of a split design, with the rotor bracket welded from steel plates, exhibiting high stiffness and low weight. The rotating shaft features a hollow structure, offering high torsional and bending stiffness while being lightweight. The entire shaft assembly is composed of two sections connected by high-strength bolts. The structure of the motor rotor is illustrated in the figure below and primarily consists of the main shaft, rotor bracket, magnetic poles, and excitation slip rings. The magnetic poles are fixed to the outer circumference of the rotor bracket with bolts, and the rotor bracket is bolted to the main shaft flange. The rotors of the two motors are fixed onto the same main shaft and supported by two shared bearings.

To assess the stiffness levels of the rotor and rotor shaft, an analysis of the stiffness and strength of the rotor core, rotor bracket, and rotor shaft was conducted. As illustrated in Fig. 21, the maximum torsional and bending stresses of the rotor shaft under the rated operating condition are 47 MPa, and the material of the rotor shaft uses forged steel 20MnSi, with a material allowance of 163.3 MPa and a safety factor of 3.46, which meets the design

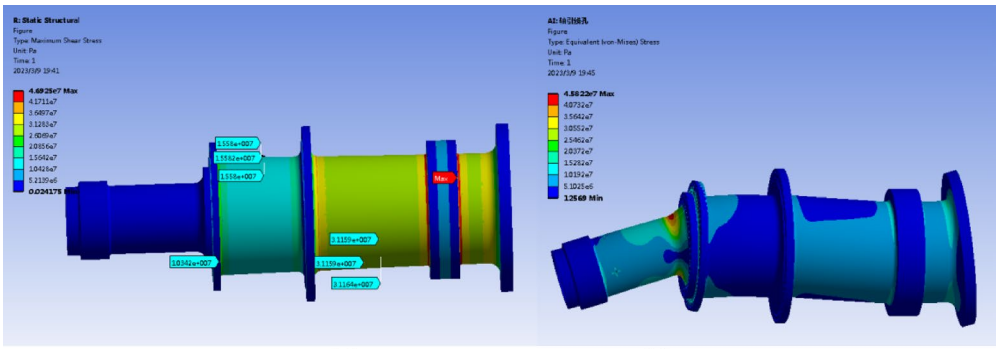

(a) (b)

Fig. 21. Stress of rotor shaft under rated condition. **a** Torsional stress. **b** Bending stress.

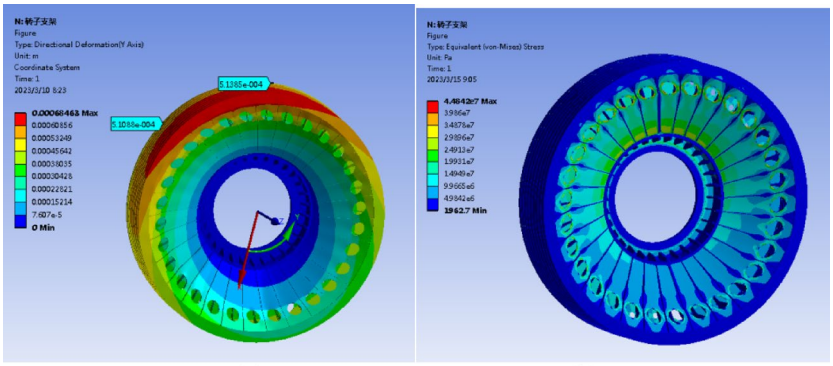

(a) (b)

Fig. 22. The deformation and stress of rotor at rated condition. **a** Deformation. **b** Stress.

Component	Operating condition	Stress	Calculated value (MPa)	Allowable value (MPa)	Safety factor
Rotor shaft	Rated torque condition	Maximum equivalent stress	32	125	3.9
	Short-circuit condition	Maximum equivalent stress	161	375	2.3
	Gravity bending + coupling load	Maximum principal stress	±47	106	2.25
Rotor bracket	Rated torque condition	Maximum equivalent stress	45	125	2.77
	Short-circuit condition	Maximum equivalent stress	222	375	1.6
	Gravity	Maximum principal stress	±21.3	96	4.6

Table 5. Results of rotor structure analysis for drag motor systems.

requirements. Figure 22 demonstrates that, the maximum deformation of the rotor core and rotor support under the rated condition is 0.7 mm, the maximum stress is 45 MPa, the rotor support material uses carbon steel Q235B, the permissible value of the material is 125 MPa, the safety factor is 2.77, to meet the requirements. Detailed results of the rotor structural analysis are presented in Table 5.

Primary mechanical failure modes include fracture and mechanical fatigue. Fracture may occur due to sudden or repeated force application. Finite element analysis confirms that the maximum equivalent stresses in both the rotor and stator comply with allowable design limits. Fatigue constitutes a critical concern for components subjected to cyclic loading, as it can initiate crack propagation and ultimately lead to structural failure. For the WFSDMs, the rotor is identified as the primary component susceptible to fatigue damage. The fatigue life of the rotor is evaluated using finite element analysis, confirming a fatigue life exceeding 1.9×10^8 cycles under cyclic loading conditions. This substantiates its structural integrity under repeated operational loads.

Conclusion

In this paper, the a staggered dual-rotor WFSDMs for offshore wind turbine full-size land-based test platform was investigated. Firstly, the theoretical model of the WFSDMs was presented and the key size parameters were calculated based on the D^2L method. A multi-objective optimization for the rotor was then conducted to increase the average torque and decrease the torque ripple. Next, the electromagnetic performance of the optimized

WFSDMs was analysed. To further mitigate the torque ripple, a staggered salient pole assembly for the dual rotor was then proposed. Finally, the structural strength of the drag motor was calibrated, and it was determined that the stator and rotor structures met safety requirements. The staggered dual-rotor WFSDM investigated in this study has been installed on the full-scale testing platform for load torque testing, and the system is currently in the equipment commissioning phase. Upon completion of commissioning, the platform will simulate marine environmental conditions to conduct: (1) Basic performance tests on the novel offshore wind turbine generator, (2) Grid fault ride-through capability tests and so on.

Data availability

All data generated or analysed during this study are included in this published article.

Received: 27 March 2025; Accepted: 28 July 2025
Published online: 20 August 2025

References

1. Jung, C. & Schindler, D. The properties of the global offshore wind turbine fleet. *Renew. Sust Energ. Rev.* **186**, 113667 (2023).
2. Li, P., Lian, J., Ma, C. & Zhang, J. Complementarity and development potential assessment of offshore wind and solar resources in China seas. *Energy. Conv. Manag.* **296**, 117705 (2023).
3. Akinbami, O. M., Oke, S. R. & Bodunrin, M. O. The state of renewable energy development in South africa: an overview. *Alex Eng. J.* **60** (6), 5077–5093 (2021).
4. Geweda, A. E. et al. Recent advances in hybrid compressed air energy storage systems: technology categorization, integration potentials with renewable energy systems, and retrofitting improvement strategies. *Alex Eng. J.* **115**, 12–29 (2025).
5. Vittori, F. et al. Model tests of a 10 MW semi-submersible floating wind turbine under waves and wind using hybrid method to integrate the rotor thrust and moments. *Wind Energy Sci.* **7** (5), 2149–2161 (2022).
6. Averous, N. R. et al. Development of a 4 MW Full-Size Wind-Turbine test bench. *IEEE J. Emerg. Sel. Top. Power Electron.* **5** (2), 600–609 (2017).
7. Zhang, D. et al. A novel full-process test bench for deep-sea in-situ power generation systems. *Energy* **297**, 1–13 (2024).
8. Giguère, P. & Wagner, J. R. Experimental verification of predicted capability of a wind turbine drivetrain test bench to replicate dynamic loads onto multi-megawatt nacelles. *Wind Eng.* **46** (4), 1047–1064 (2022).
9. Prévost, A., Léchappé, V., Delpoux, R. & Brun, X. An emulator for static and dynamic performance evaluation of small wind turbines. In *The IEEE International Symposium on Industrial Electronics* (2023).
10. Rohr, A. & Jauch, C. Large scale test bench for emulating grid connected wind turbines of different sizes. In *2019 IEEE 13th International Conference on Compatibility, Power Electronics and Power Engineering*, CPE-POWERENG (2019).
11. Mohammadi, E., Fadaeinedjad, R. & Naji, H. R. Platform for design, simulation, and experimental evaluation of small wind turbines. *IET Renew. Power Gener*. **13** (9), 1576–1586 (2019).
12. Ding, Y., Zhou, L. & Yang, J. Inertia compensation strategy of wind turbine drivetrain testing facility based on energy flow equivalence. In *2023 8th Asia Conference on Power and Electrical Engineering*, ACPEE 1425–1430 (2023).
13. Mohammadi, E., Fadaeinedjad, R. & Moschopoulos, G. An electromechanical emulation-based study on the behaviour of wind energy conversion systems during short circuit faults. *Energy Conv. Manag.* **205**, 1–15 (2020).
14. Xie, J. et al. Characteristics simulation method of megawatt Three-Blade horizontal axis wind turbine based on laboratory kilowatt Low-Power motor system. *IEEE Trans. Ind. Appl.* **58** (1), 645–655 (2022).
15. Mohammadi, E., Fadaeinedjad, R., Naji, H. R. & Moschopoulos, G. Investigation of horizontal and vertical wind shear effects using a wind turbine emulator. *IEEE Trans. Sustain. Energy*. **10** (3), 1206–1216 (2019).
16. Jaenudin, J., Sandi, M. D. & Hendriko, H. Development of a simulator for steam turbine generator protection system based on a distributed control system. *J. Eur. Systèmes Autom.* **57** (5), 1329–1336 (2024).
17. Grune, R. & Geske, M. A discussion on the characterization of grid emulators by apparent power rating and short-circuit power, forsch. *Im Ingenieurwes.* **87** (1), 309–319 (2023).
18. Emamalipour, R. & Lam, J. String-Inverter/Rectifier Soft-Switched bidirectional DC/DC converter. *IEEE Trans. Power Electron.* **35** (8), 8200–8214 (2020).
19. Li, D. et al. Multi-Degree-of-Freedom load reproduction by electrohydraulic Digital-Servo loading for wind turbine drivetrain. *Energies* **16** (12), 4659 (2023).
20. de Oliveira, C. M. R. et al. High-Accuracy dynamic load emulation method for electrical drives. *IEEE Trans. Ind. Electron.* **67** (9), 7239–7249 (2020).
21. Usha, S., Geetha, P., Geetha, A. & Palanisamy, R. Performance enhancement of sensorless induction motor drive using modified direct torque control techniques for traction application. *Alex Eng. J.* **108**, 518–538 (2024).
22. Meng, D., Wu, Q., Zhang, J., Li, Y. & Diao, L. Restarting control of free-running interior permanent magnet synchronous motor under position sensorless control. *Alex Eng. J.* **115**, 83–93 (2025).
23. Shaikh, M. F., Park, J., Park, Y., Lee, S. B. & Antonino-Daviu, J. A. Electrical testing for detection and classification of open damper bar and shorted field winding failures in wound field synchronous motors. *IEEE Trans. Ind. Appl.* **58** (4), 4532–4541 (2022).
24. Graffeo, F., Vaschetto, S., Rubino, S., Tenconi, A. & Cavagnino, A. Fast computation of the no-load characteristic for wound field synchronous propulsion motors. *IEEE Trans. Transport. Electrific.* **11** (1), 4111–4120 (2025).
25. Habib, A. et al. Predictive current control based Pseudo six-phase induction motor drive. *Alex Eng. J.* **61** (5), 3937–3948 (2022).
26. Siregar, Y., Siahaan, Y. R. O., Mohamed, N. N. B., Riawan, D. C. & Yuhendri, M. Design of starting a three phase induction motor using direct on-line, variable frequency drive, soft starting, and auto transformer methods. *Indones J. Electr. Eng. Comput. Sci.* **37** (2), 700–714 (2025).
27. Mohamed, M. Y. et al. Optimized design of a fault-tolerant 12-slot/10-pole six-phase surface permanent magnet motor with asymmetrical winding configuration for electric vehicles. *Alex Eng. J.* **110**, 527–539 (2025).
28. Hassan, A. A., El-Sawy, A. M., Mohamed, Y. S. & Shehata, E. G. Sensorless sliding mode torque control of an IPMSM drive based on active flux concept. *Alex Eng. J.* **51** (1), 1–9 (2012).
29. Oh, H. et al. Performance improvement of wound field synchronous motor for EV propulsion applying grain oriented electrical steel. *IEEE Trans. Magn.* **61** (2), 1–4 (2025).
30. Wibisono, F. I. & Asama, J. Wound field synchronous motor using a Non-Salient pole rotor with distributed winding. In *2023 IEEE Energy Conversion Congress and Exposition* (ECCE), Oct. 4030–4033 (2023).
31. Bukhari, S. S. H., Sirewal, G. J., Ayub, M. & Ro, J. S. A new Small-Scale Self-Excited wound rotor synchronous motor topology. *IEEE Trans. Magn.* **57** (2), 1–5 (2021).
32. Kasaei, W., Yang, Z., Wang, J. & Yan Advancements and applications of Rim-Driven fans in aerial vehicles: A comprehensive review. *Appl. Sci.* **13** (22), 12502 (2023).

Acknowledgements
This work was supported by the National Key Research and Development Program of China under Grant 2022YFB2402800.

Author contributions
Y.X., S.Q. and N. W. wrote the main manuscript text, C.Q. and C. L.prepared Figs. 1, 14, 16 and 17, and Tables 1, 2, 3, 4 and 5, W.Z. and N. W. aprepared Figs. 2, 3, 4, 5, 6, 7, 8, 9, 10, 11, 12, 13, 15, 18, 19, 20, 21 and 22. All authors reviewed the manuscript.

Declarations

Competing interests
The authors declare no competing interests.

Additional information
Correspondence and requests for materials should be addressed to W.Z.

Reprints and permissions information is available at www.nature.com/reprints.

Publisher's note Springer Nature remains neutral with regard to jurisdictional claims in published maps and institutional affiliations.